Rotor Angle Stability Prediction of Power Systems with High Wind Power Penetration Using a Stability Index Vector

Yuchuan Chen, Seyed Mahdi Mazhari, *Member*, *IEEE*, C.Y. Chung, *Fellow*, *IEEE*, Sherif O. Faried, *Senior Member*, *IEEE*, and Bikash C. Pal *Fellow*, *IEEE*

***Abstract*—This paper proposes a methodology for predicting online rotor angle stability in power system operation under significant contribution from wind generation. First, a novel algorithm is developed to extract a stability index (*SI*) that quantifies the margin of rotor angle stability of power systems reflecting the dynamics of wind power. An approach is proposed that takes advantage of the machine learning technique and the newly defined *SI*. In case of a contingency, the developed algorithm is employed in parallel to find *SI*s for all possible instability modes. The *SI*s are formed as a vector and then applied to a classifier algorithm for rotor angle stability prediction. Compared to other features used in state-of-the-art methods, *SI* vectors are highly recognizable and thus can lead to a more accurate and reliable prediction. The proposed approach is validated on two IEEE test systems with various wind power penetration levels and compared to existing methods, followed by a discussion of results.**

***Index Terms*—Decision tree, extended equal-area criterion, machine learning, phasor measurement units, rotor angle stability, stability index, wind power plants.**

I. Introduction

ROTOR angle stability is the ability of a synchronized power system to maintain synchronism when subjected to a contingency. Historically, large-disturbance rotor angle instability has been the most severe stability challenge for most systems [1]. Fast prediction of potential instabilities allows more time for remedial actions and prevents unintended islanding and widespread blackouts.

Many techniques have been proposed for rotor angle stability prediction. Among them, time-domain simulation is one of the most reliable approaches [2], in which power system dynamic models are represented by differential equations and solved numerically at each time instant. The simulation needs to be conducted immediately after the fault and demands complete information of the grid and the fault. However, this method may require long post-fault observation windows, which subsequently increases the prediction time for online applications [3]. Another rotor angle stability prediction approach is related to the Lyapunov stability-based transient energy function [4]–[8], in which kinetic and potential energies are evaluated for a post-fault system. Transient energy function methods perform well in terms of computation speeds, but still face challenges with respect to applications to renewable-energy-connected systems [9] and accuracy improvement. The third popular approach is machine learning (ML)-based techniques, which make online rotor angle stability prediction using real-time synchronized data obtained by phasor measurement units (PMUs) [3], [10]–[12]. Generally, ML-based techniques require a large set of labeled data obtained by offline simulations for model training, during which the diverse scenarios that can take place in power systems are enumerated. Notably, these prediction methods have advantages in terms of calculation speed and are more adaptable to bulk power systems in this respect. However, in the presence of the high penetration of wind powers, the transient stability characteristic of the system also evolves, so ML-based prediction accuracy may be affected.

First, the output of wind power plants (WPPs) can vary both temporally and spatially [13], which exponentially increases the possible system pre-fault operation scenarios and imposes multi-source uncertainties to the overall system dynamics [9]. Consequently, extensive training data may be required to cope with the combination of all possible uncertainties in power systems, and as such the computation time explodes [9]. Handling a high volume of data entails more sophisticated prediction models and a larger number of features. In addition, it may boost the dimensionality of the input space and further increases the chance of overfitting and affects the overall performance [14]. However, an algorithm that demands massive offline data restricts the updating process of the prediction models. Consequently, the generalization ability of such prediction models is restricted, and the deficiencies noted may impede the application of ML-based methods to real-life projects.

In addition, exploring informative and discriminative features is crucial for ML-based methods to reach reliable prediction models. As uncertainties of the system increase, existing features such as bus voltages [3], [10]–[12], which are obtained via PMU measurements, may no longer be so useful. A few post-fault samples of these raw data may be unable to intuitively reflect the effects of dispersed WPPs and their uncertainties on system dynamics, as several possible combinations of uncertainties may lead to similar values. Interpreting these raw data into derived features that better represent the underlying problem can help improve model accuracy on test data.

Moreover, most of the ML-based studies mentioned above utilize post-fault data obtained after fault clearance for stability prediction, which postpones the forecasting phase. Considering new advancements in PMU development, measurement data are now reliable and consistent during transients [15]. Therefore, the reduction of these data might be of interest when considering the importance of quick action against instability.

Aimed at unraveling the above-mentioned restrictions, a novel rotor angle stability prediction method is proposed. In this method, a rotor angle stability index (*SI*) is developed, in which WPPs are represented as variable dynamic admittances to be integrated into

This work was supported in part by the Natural Sciences and Engineering Research Council (NSERC) of Canada and the Saskatchewan Power Corporation (SaskPower).

Y. Chen, S.M. Mazhari, C.Y. Chung, and S.O. Faried are with the Department of Electrical and Computer Engineering, University of Saskatchewan, Saskatoon S7N 5A9, Canada (e-mail: yc.chen@usask.ca; s.m.mazhari@usask.ca; c.y.chung@usask.ca; sof280@mail.usask.ca;).

Bikash. C. Pal is with the Control and Power Group, Department of Electrical and Electronic Engineering, Imperial College London, London, SW7 2BT, U.K. (e-mail: b.pal@imperial.ac.uk).

an equivalent network model during the transients. To calculate the energy without integral operation, a short-term terminal voltage recovery trajectory is derived for each WPP. In this way, the effects of WPPs on kinetic and potential energies of a system are calculated after disturbances. Given the developed SI, an $\boldsymbol{SI}$ vector is proposed, which consists of the SI values of an overall set of instability modes (IMs) of a certain system. Thereafter, the $\boldsymbol{SI}$ vector can be rapidly computed following a contingency and used as a feature applied to an ensemble classifier algorithm, which demonstrates a superior prediction performance. The performance of the proposed method is evaluated in IEEE 68-bus and 300-bus test system models and compared with other existing methods.

II. Extended Equal Area Criterion (EEAC)

Multiple transient energy function-based rotor angle stability assessment methods were widely discussed in the 1980s [4]–[8] for transient security analysis. In this study, a novel *SI* algorithm inspired by the EEAC is further explored for power systems with WPPs.

The EEAC is developed for a system with n synchronous generators (SGs) [8]. In EEAC, the SGs are grouped into two complementary clusters by IM identification: the critical SGs that cause loss of synchronism and the remaining SGs, denoted as S and A, respectively. These clusters are then modeled by two equivalent machines so that each represents the dynamics of the corresponding machines within a partial center of angles frame. The system is further reduced to a one-machine-infinite-bus (OMIB) system. The mapping of the equivalent OMIB under such clustering is given by (1)–(5) [8], [16]:

$$\delta = \delta_S - \delta_A, \quad \frac{M}{\omega_0}\dot{\omega} = P_m - P_e \tag{1}$$

$$\delta_S = \frac{1}{M_S}\sum_{i\in S}\delta_i M_i, \quad \delta_A = \frac{1}{M_A}\sum_{j\in A}\delta_j M_j \tag{2}$$

$$M = \frac{M_S M_A}{M_T}, M_T = M_S + M_A, \ M_S = \sum_{i\in S} M_i\,,\ M_A = \sum_{j\in A} M_j \tag{3}$$

$$P_m = \frac{1}{M_T}\left(M_A \sum_{i\in S} P_{mi} - M_S \sum_{j\in A} P_{mj} \right) \tag{4}$$

$$P_e = \frac{1}{M_T}\left(M_A \sum_{i\in S} P_{ei} - M_S \sum_{j\in A} P_{ej} \right) \tag{5}$$

where δ_i and M_i represent the rotor angle and inertia of the i^{th} SG, respectively. In a similar manner, δ and M stand for the same values related to the equivalent OMIB system, and ω_0 is synchronous speed. Subscripts S and A indicate the corresponding electrical quantities of the equivalent SG in the partial center of angles frame. P_m and P_e are the mechanical and electrical power of the equivalent OMIB, respectively. Then the system is reduced at the generator internal nodes to a network equivalent, and with an additional simplification for machines within clusters S and A [8]:

$$\delta_i \approx \delta_S \mid \forall i \in S\,, \qquad \delta_j \approx \delta_A \mid \forall j \in A \tag{6}$$

the active power output of the i^{th} SG can be expressed by [16]:

$$\begin{aligned} P_{ei} = \mathrm{Re}\left(\vec{E}_i \vec{I}_i^*\right) = \ & E_i \boldsymbol{\varepsilon}_i^{\mathrm{T}} \mathrm{Re}(\boldsymbol{Y}_{SS})\boldsymbol{E}_S + \\ & E_i \boldsymbol{\varepsilon}_i^{\mathrm{T}}[\sin\delta\, \mathrm{Im}(\boldsymbol{Y}_{SA}) + \cos\delta\, \mathrm{Re}(\boldsymbol{Y}_{SA})]\boldsymbol{E}_A \end{aligned} \tag{7}$$

where $\vec{E}_i$ and $\vec{I}_i$ represent the complex voltage and current injections of the internal node of the i^{th} SG, $\boldsymbol{\varepsilon}_i$ is a standard basis in $\mathbb{R}^{|S|}$, and $\vec{\boldsymbol{E}}_S$ and $\vec{\boldsymbol{E}}_A$ indicate complex voltage column vectors of SG internal nodes in sets S and A, respectively. $\boldsymbol{Y}_{SS}$ and $\boldsymbol{Y}_{AA}$ denote self-admittance of SG internal nodes in sets S and A, respectively. E_i is the magnitude of $\vec{E}_i$, and $\boldsymbol{E}_S$ and $\boldsymbol{E}_A$ are column vectors that include the magnitudes of each element in $\vec{\boldsymbol{E}}_S$ and $\vec{\boldsymbol{E}}_A$, respectively. P_{ej} is expressed similarly. For simplicity, $\boldsymbol{E}_S$, $\boldsymbol{E}_A$, and P_m are assumed to maintain their steady-state values during transients [8]. Thus, P_e in (5) can be obtained by (8)–(9) [16]:

$$P_e = P_C + P_{max}\sin(\delta - \gamma) \tag{8}$$

$$P_C = \tfrac{M_A}{M_T}\boldsymbol{E}_S{}^{\mathrm{T}}\mathrm{Re}(\boldsymbol{Y}_{SS})\boldsymbol{E}_S + \tfrac{M_S}{M_T}\boldsymbol{E}_A{}^{\mathrm{T}}\mathrm{Re}(\boldsymbol{Y}_{AA})\boldsymbol{E}_A \tag{9}$$

where both P_{max} and γ are constants [16]. Then, the "accelerating area" and "decelerating area" of the equivalent OMIB system, which respectively correspond to the kinetic and potential energies of the system, are calculated using:

$$A_{acc} = \int_{\delta(t_{\mathrm{f}})}^{\delta(t_{\mathrm{c}})} (P_m - P_{e_D}(\delta))d\delta \tag{10}$$

$$A_{dec} = \int_{\delta(t_{\mathrm{c}})}^{\delta(t_{\mathrm{u}})} (P_{e_P}(\delta) - P_m)d\delta \tag{11}$$

where subscripts D and P respectively represent the system electric quantities during and after the clearance of faults; t_{f} and t_{c} respectively stand for fault time and fault clearance time; and t_{u} is the time instant when the system reaches the unstable equilibrium point. The calculation of $\delta(t_{\mathrm{u}})$ is introduced in [16]. In this method, the stability of the system is judged by comparing the difference between kinetic and potential energy against a predefined threshold value.

III. Derivation of a Novel Stability Index

To address the challenges faced by *SI* calculation caused by WPP dynamics, a novel algorithm inspired by the EEAC for calculating *SI* is introduced in this section. First, the calculation of a set of virtual dynamic admittances to reshape the systems and model the dynamic behavior of WPPs is introduced in Section III.A. Impacts of WPPs on the electromagnetic power of SGs are then analyzed in Section III.B. Finally, the short-term terminal voltage recovery of WPPs is derived in Section III.C and, consequently, a novel *SI* considering the dynamics of WPPs is put forward.

A. Dynamic Equivalence of WPPs

The principle of dynamic admittances is used to eliminate WPP nodes while retaining their transient effects on SGs. Consider a network with two SGs and one WPP, as shown in Fig. 1, which is reduced at the SG internal nodes and point of intersection (POI) of the WPP in the equivalent network model. Because $\vec{I}_1$ and $\vec{I}_2$ should be consistent with the corresponding values after WPP elimination, the dynamic equivalent admittances Y_1' and Y_2' are obtained in (12):

$$Y_1' = \left(1 - \tfrac{\vec{V}_W}{\vec{E}_1}\right)Y_1, \ Y_2' = \left(1 - \tfrac{\vec{V}_W}{\vec{E}_2}\right)Y_2 \tag{12}$$

Similarly, consider a system with n SGs and n' WPPs; an electrical equivalent of the system is constructed, as shown in Fig. 2 (a). Generally, the wind generators (WGs) in WPPs are not synchronously connected to the grid, and thus do not face rotor angle instability. However, the power output from these WPPs during transient conditions is affected by network voltage, which in turn affects the rotor angle stability of the system [9]. In dynamic coherency determination studies [17], each non-SG bus, including POIs [17], is appended to an associated SG coherent group to form a coherent area following a disturbance. This is determined by the rate of change of voltage angle or frequency-deviation signals of each bus [17]. Accordingly, the POIs with connected WPPs are divided into two complementary clusters—critical subset G and the remaining subset H, which are appended to the S and A groups, respectively—as shown in Fig. 2(a).

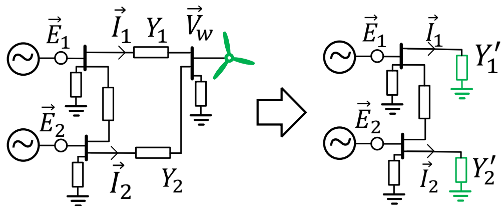

Fig. 1. The principle of dynamic admittances.

The equivalent network is given in (13), where $\vec{\boldsymbol{I}}_S$ and $\vec{\boldsymbol{I}}_A$ represent complex current column vectors of SG internal nodes in sets S and A, respectively. $\vec{\boldsymbol{V}}_G$, $\vec{\boldsymbol{I}}_G$ and $\vec{\boldsymbol{V}}_H$, $\vec{\boldsymbol{I}}_H$ are the complex voltage and current column vectors of POIs in sets G and H, respectively. What remains is the admittance matrix, in which the diagonal and non-diagonal elements are the self and mutual admittances of the network, respectively.

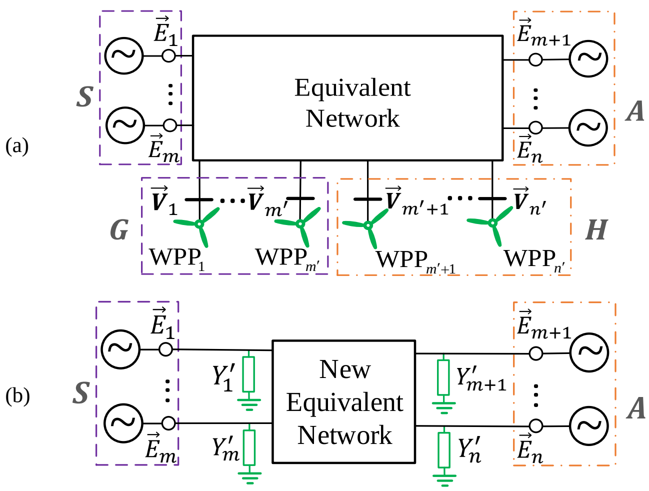

Fig. 2. Dynamic equivalence of WPPs.

Similar to Fig. 1, a series of dynamic admittances that act as additional self-impedance of each internal node can be built to simulate the transient behavior of WPPs, as shown in Fig. 2(b), during which the network in Fig. 2(a) is first reduced at the generator internal nodes and POIs, and the principle of dynamic admittance introduced in Fig. 1 is then applied. Thus, the equivalent network of Fig. 2(a) is rebuilt; the WPP nodes are eliminated and the connections between each SG remain the same. The current-injection model of the system in Fig. 2(b) is given by (14):

$$\begin{bmatrix} \vec{\boldsymbol{I}}_S \\ \vec{\boldsymbol{I}}_G \\ \vec{\boldsymbol{I}}_A \\ \vec{\boldsymbol{I}}_H \end{bmatrix} = \begin{bmatrix} \boldsymbol{Y}_{SS} & \boldsymbol{Y}_{SG} & \boldsymbol{Y}_{SA} & \boldsymbol{Y}_{SH} \\ \boldsymbol{Y}_{GS} & \boldsymbol{Y}_{GG} & \boldsymbol{Y}_{GA} & \boldsymbol{Y}_{GH} \\ \boldsymbol{Y}_{AS} & \boldsymbol{Y}_{AG} & \boldsymbol{Y}_{AA} & \boldsymbol{Y}_{AH} \\ \boldsymbol{Y}_{HS} & \boldsymbol{Y}_{HG} & \boldsymbol{Y}_{HA} & \boldsymbol{Y}_{HH} \end{bmatrix} \begin{bmatrix} \vec{\boldsymbol{E}}_S \\ \vec{\boldsymbol{V}}_G \\ \vec{\boldsymbol{E}}_A \\ \vec{\boldsymbol{V}}_H \end{bmatrix} \tag{13}$$

$$\begin{bmatrix} \vec{\boldsymbol{I}}_S \\ \vec{\boldsymbol{I}}_A \end{bmatrix} = \begin{bmatrix} \boldsymbol{Y}'_{SS} & \boldsymbol{Y}_{SA} \\ \boldsymbol{Y}_{AS} & \boldsymbol{Y}'_{AA} \end{bmatrix} \begin{bmatrix} \vec{\boldsymbol{E}}_S \\ \vec{\boldsymbol{E}}_A \end{bmatrix} \tag{14}$$

where

$$\boldsymbol{Y}'_{SS} = \boldsymbol{Y}_{SS} + \mathrm{diag}[Y'_1, \dots, Y'_m] \tag{15}$$

$$\boldsymbol{Y}'_{AA} = \boldsymbol{Y}_{AA} + \mathrm{diag}[Y'_{m+1}, \dots, Y'_n] \tag{16}$$

and $Y'_1, \dots, Y'_m, Y'_{m+1}, \dots, Y'_n$ are dynamic admittances. Similar to (12), these admittances are calculated by:

$$Y'_i = \sum_{g \in G} \left[\left(1 - \frac{\vec{V}_g}{\vec{E}_i} \right) Y_{ig} \right] + \sum_{h \in H} \left[\left(1 - \frac{\vec{V}_h}{\vec{E}_i} \right) Y_{ih} \right] \tag{17}$$

where $i \in S \cup A$.

It can be seen from (17) that the dynamic equivalent admittances can reflect the effect of uncertainties of wind power; as the voltages of SG internal nodes and POIs fluctuate with wind power generation, the admittances change accordingly.

Therefore, during fault-free conditions, the values of the dynamic equivalent admittances vary at all times due to the wind speed uncertainties. During transients, the wind speeds of each WPP are assumed to remain constant [18] (assuming they start when a fault occurs t_{f} and end at 1–5s after fault clearance t_{c}); thus, the dynamic change of these admittances are determined by the pre-fault conditions and the transient process of the system, including the fault-related change of system states, variables, and topology, the controls on WPPs, etc.

B. Electromagnetic Power of SGs Considering WPPs

After the inclusion of the dynamic admittances shown in Fig. 2(b), P_{ei} in (7) and P_e in (8) are rewritten in which $\boldsymbol{Y}_{SS}$ and $\boldsymbol{Y}_{AA}$ are respectively replaced by $\boldsymbol{Y}'_{SS}$ and $\boldsymbol{Y}'_{AA}$. From (15)–(16), $\boldsymbol{Y}'_{SS}$ and $\boldsymbol{Y}'_{AA}$ are composed of self and mutual admittances of the SGs and the dynamic admittances; hence, for the WPP-integrated power system, the electromagnetic power of each SG includes the amount exchanged among the SGs as well as among the SGs and the WPPs. Similar to (6), because the dynamics of the voltage angles of buses within one coherent group are similar [17], an assumption is made for the unstable cases. During the period after t_{c}, it has

$$\theta_g \approx \delta_S \mid \forall g \in G\,,\ \theta_h \approx \delta_A \mid \forall h \in H \tag{18}$$

where θ_g and θ_h represent the voltage angle of POI g and h, respectively; thus, (17) is further simplified. Therefore, the variables remaining in P_e are δ and $\boldsymbol{V}$, where $\boldsymbol{V} = [\boldsymbol{V}_G^{\mathrm{T}}\ \boldsymbol{V}_H^{\mathrm{T}}]^{\mathrm{T}}$, and $\boldsymbol{V}_G$ and $\boldsymbol{V}_H$ are column vectors that include the magnitudes of each element in $\vec{\boldsymbol{V}}_G$ and $\vec{\boldsymbol{V}}_H$, respectively. Because δ is the variable of the integration of (10) and (11), if the δ–$\boldsymbol{V}$ relationship of the post-fault function is obtained, then the antiderivative of (10) and (11) can be derived, which leads to the calculation of kinetic and potential energies without an integral operation.

C. Proposed SI Considering WPPs

1) Post-Fault Recovery of $\boldsymbol{V}$

During the fault period, t_{f} to t_{c}, the dip values of $\boldsymbol{V}$ are obtainable from PMUs and can be used for kinetic energy calculation. Thereby, the remaining challenge to calculate potential energy is to derive the potential $\boldsymbol{V}$ - δ relationship during t_{c} to t_{u}, defined as t_{cu}.

In this study, all WGs are considered to be doubly-fed induction generators (DFIGs) due to their popularity among current WPPs. All WGs are assumed to have fault ride-through capability and remain connected during faults, and are involved in Volt/VAR control to regulate the voltage of their respective POIs; this is the most prevalent output control in recent North American and European WPPs [18]. The methodology introduced below can be modified for application to DFIGs under other output control situations.

Faster-acting local controls implemented in the WG converters can provide a dynamic response to voltage dips. The introduction of a generator/converter model of DFIG that regulates real and reactive power output is reported in [19]. Denote V_w as the voltage magnitude of the POI of the w^{th} WPP. During the V_w drop period, the delivery of reactive power of this WPP, Q_w, is given priority by the Volt/VAR control. In other words, the active power P_w remains limited while Q_w increases to support V_w recovery. This control mode is generally triggered from t_{f} and continues after fault clearance if $V_w(t_{\text{c}+})$ fails to recover immediately; Q_w then increases and remains at its maximum output until V_w recovers. This process is illustrated in Fig. 3, in which the WPP is in full rated output (100 MW) before the contingency. Similar simulation results are also reported in [20] and [21].

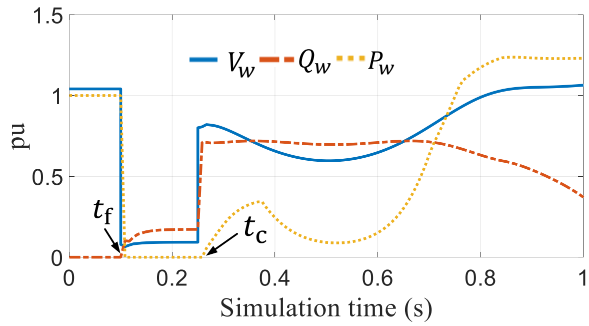

Fig. 3. Real power, reactive power, and terminal voltage of a Volt/VAR controlled WPP.

The control strategy of WGs affects their regulated voltages $\boldsymbol{V}$ and reactive power outputs $\boldsymbol{Q}$, which consequently influence the dynamics of the system. In light of this structure, a $\boldsymbol{V}$ - δ relationship can be obtained by a derivative operator by having an idea about the transient characteristics of $\boldsymbol{Q}$. To this end, denote:

$$V_w(t_{\text{cu}}) \ = V_w(t_{\text{f}-}) \mid \forall\, w \in G \cup H, V_w(t_{\text{c}+}) \geq \varphi V_w(t_{\text{f}-}) \qquad (19)$$

where $V_w(t_{\text{cu}})$ represents V_w during t_{cu}, $V_w(t_{\text{f}-})$ is equal to V_w at steady state, and φ is a threshold ratio of $V_w(t_{\text{c}+})$ to $V_w(t_{\text{f}-})$. Equation (19) means that V_w is almost immediately recovered after t_{c} if $V_w(t_{\text{c}+})$ reaches close to its pre-fault value. Specifically, φ is set to 0.9 because this is the typical value to trigger the low voltage condition of Volt/VAR control in WPPs.

On the other hand, for those $V_w(t_{\text{c}+})$ that fail to reach $\alpha V_w(t_{\text{f}-})$, according to the Volt/VAR control in DFIGs, the corresponding WPP would increase its reactive power output and remain at its maximum limitation until the voltage is restored. Hence, during t_{cu}, the reactive outputs of those WPPs can be considered as:

$$Q_w = \bar{Q}_w \quad \mid \forall\, w \in G \cup H \,,\ V_w(t_{\text{c}+}) < \varphi V_w(t_{\text{f}-}) \qquad (20)$$

where $\bar{Q}_w$ is the maximum reactive output of the w^{th} WPP, which is considered as a constant and determined by the controllers of the WGs in the WPP [18].

The reactive power outputs of each WPP are constructed by:

$$\boldsymbol{Q} = [\boldsymbol{Q}_G^{\text{T}} \ \ \boldsymbol{Q}_H^{\text{T}}]^{\text{T}} \qquad (21)$$

where $\boldsymbol{Q}_G$ and $\boldsymbol{Q}_H$ represent reactive power injection column vectors of WPPs of sets G and H, respectively. Given (13), (17), and (18), $\boldsymbol{Q}_G$ can be derived as (22), where $\otimes$ is pointwise multiplication; and $\boldsymbol{Q}_H$ is expressed in a similar way.

$$\begin{aligned}&\boldsymbol{Q}_G = \operatorname{Im}(\vec{\boldsymbol{V}}_G \otimes \vec{\boldsymbol{I}}_G^*) = \\ &-\boldsymbol{V}_G \otimes \begin{pmatrix} \operatorname{Im}(\boldsymbol{Y}_{GG})\boldsymbol{V}_G + \cos\delta\,(\operatorname{Im}(\boldsymbol{Y}_{GH})\boldsymbol{V}_H + \operatorname{Im}(\boldsymbol{Y}_{GA})\boldsymbol{E}_A) \\ +\operatorname{Im}(\boldsymbol{Y}_{GS})\boldsymbol{E}_S - \sin\delta(\operatorname{Re}(\boldsymbol{Y}_{GH})\boldsymbol{V}_H + \operatorname{Re}(\boldsymbol{Y}_{GA})\boldsymbol{E}_A)\end{pmatrix}\end{aligned} \qquad (22)$$

From (22), $\boldsymbol{Q}$ is a function of $\boldsymbol{V}$ and δ. From (19), V_w can be considered a constant value after t_{c} if $V_w(t_{\text{c}+}) \geq \varphi V_w(t_{\text{f}-})$; so, we only need to focus on those $\{V_w, Q_w \mid \forall\, w \in G \cup H, V_w(t_{\text{c}+}) < \varphi V_w(t_{\text{f}-})\}$ for the derivation of the $\boldsymbol{V}$ - δ relationship during t_{cu}. These voltages and reactive power are constructed by:

$$\begin{aligned}\boldsymbol{V}' = [V_1 \cdots V_w \cdots V_{n'}]^{\text{T}}, \boldsymbol{Q}'(\boldsymbol{V},\delta) = [Q_1 \cdots Q_w \cdots Q_{n'}]^{\text{T}} \mid \ \forall\, w \\ \in G \cup H \,, V_w(t_{\text{c}+}) < \varphi V_w(t_{\text{f}-})\end{aligned} \qquad (23)$$

During t_{cu}, (19) shows that:

$$\Delta V_w = 0 \ \ \mid \forall\, w \in G \cup H \ \ , \ \ V_w(t_{\text{c}+}) \geq \varphi V_w(t_{\text{f}-}) \qquad (24)$$

and thus $\boldsymbol{Q}'$ in (23) can be rewritten as $\boldsymbol{Q}'\left(\boldsymbol{V}', \delta\right)$.

Further, (20) shows that $\boldsymbol{Q}'$ in (23) is a constant column vector during t_{cu} and, thus, ignoring higher order terms during t_{cu} leads to:

$$\left[\frac{\partial \boldsymbol{Q}'(\boldsymbol{V}',\delta)}{\partial(\boldsymbol{V}',\delta)}\right]\Bigg|_{\boldsymbol{V}'=\boldsymbol{V}'(t_{\text{c}+}),\ \ \delta=\delta(t_{\text{c}})} \begin{bmatrix}\Delta \boldsymbol{V}' \\ \Delta\delta\end{bmatrix} = \boldsymbol{0} \qquad (25)$$

where $\left[\frac{\partial \boldsymbol{Q}'(\boldsymbol{V}',\delta)}{\partial(\boldsymbol{V}',\delta)}\right]$ is a Jacobian matrix. Thus, from (25), a linear relation between $\boldsymbol{V}'$ and δ can be obtained by (26) during t_{cu}:

$$\Delta \boldsymbol{V}' = \boldsymbol{K}' \Delta\delta \qquad (26)$$

where $\boldsymbol{K}'$ are linear coefficients between $\Delta \boldsymbol{V}'$ and $\Delta\delta$ during t_{cu}:

$$\boldsymbol{K}' = -\left[\frac{\partial(\boldsymbol{Q}')}{\partial(\boldsymbol{V}')}\right]^{-1} \left[\frac{\partial(\boldsymbol{Q}')}{\partial\delta}\right]\Bigg|_{\boldsymbol{V}'=\boldsymbol{V}'(t_{\text{c}+}),\ \ \delta=\delta(t_{\text{c}})} \qquad (27)$$

For generalization, $\boldsymbol{V}(t_{cu})$ can be written as:

$$\boldsymbol{V}(t_{cu}) = \left[\boldsymbol{V}_G^{\text{T}}(t_{\text{c}+}) \ \ \boldsymbol{V}_H^{\text{T}}(t_{\text{c}+})\right]^{\text{T}} + \left[\boldsymbol{K}_G^{\text{T}} \ \ \boldsymbol{K}_H^{\text{T}}\right]^{\text{T}}(\delta - \delta_{\text{c}}) \qquad (28)$$

where $\left[\boldsymbol{K}_G^{\text{T}} \ \ \boldsymbol{K}_H^{\text{T}}\right]^{\text{T}}$ is the linear coefficient between $\Delta\boldsymbol{V}$ and $\Delta\delta$ during t_{cu}. In particular:

$$\begin{aligned}V_w(t_{\text{c}+}) \ = V_w(t_{\text{f}-}),\ K_w = 0 \mid \forall\, w \in G \cup H, V_w(t_{\text{c}+}) \\ \geq \varphi V_w(t_{\text{f}-})\end{aligned} \qquad (29)$$

and other K_w in $\left[\boldsymbol{K}_G^{\text{T}} \ \ \boldsymbol{K}_H^{\text{T}}\right]^{\text{T}}$ are calculated from (28). Relying on (28), the $\boldsymbol{V}$ - δ relationship is obtained. A novel *SI*, derived from that, is proposed next.

2) Proposed SI

Given (8)–(9), (15)–(18), and (28), the integrals in (30) and (31), which respectively correspond to the kinetic and potential energies of a system after fault clearance considering WPPs, can be obtained:

$$A_{acc} = \int_{\delta(t_{\text{f}})}^{\delta(t_{\text{c}})} (P_m - P_{e_D}(\delta))d\delta = A_{acc1} + A_{acc2} \qquad (30)$$

$$A_{dec} = \int_{\delta(t_{\text{c}})}^{\delta(t_{\text{u}})} (P_{e_P}(\delta) - P_m)d\delta = A_{dec1} + A_{dec2} \qquad (31)$$

where

$$\begin{aligned}A_{acc1} = \left(P_m - P_{C_D}\right)(\delta(t_{\text{c}}) - \delta(t_{\text{f}})) + \\ P_{\max_D}(\cos(\delta(t_{\text{c}}) - \gamma_D) - \cos(\delta(t_{\text{c}}) - \gamma_D))\end{aligned} \qquad (32)$$

$$\begin{aligned}A_{acc2} = \xi_1(\delta(t_{\text{c}}) - \delta(t_{\text{f}})) + \xi_2(\sin\delta(t_{\text{c}}) - \sin\delta(t_{\text{f}})) \\ - \xi_3(\cos\delta(t_{\text{c}}) - \cos\delta(t_{\text{f}}))\end{aligned} \qquad (33)$$

$$\begin{aligned}A_{dec1} = \left(P_{C_P} - P_m\right)\left(\delta(t_{\text{u}}) - \delta(t_{\text{c}})\right) + \\ P_{\max_P}\cos(\delta(t_{\text{c}}) - \gamma_P) - P_{\max_P}\cos(\delta(t_{\text{u}}) - \gamma_P)\end{aligned} \qquad (34)$$

$$\begin{aligned} A_{dec2} = \eta_1\big(\delta(t_{\mathrm{u}}) - \delta(t_{\mathrm{c}})\big) + \eta_2\big(\delta^2(t_{\mathrm{u}}) - \delta^2(t_{\mathrm{c}})\big) \\ + (\eta_3 + \eta_6)(\sin\delta(t_{\mathrm{u}}) - \sin\delta(t_{\mathrm{c}})) \\ + (\eta_4 + \eta_5)(\cos\delta(t_{\mathrm{u}}) - \cos\delta(t_{\mathrm{c}})) \\ + \eta_5(\delta(t_{\mathrm{u}})\sin\delta(t_{\mathrm{u}}) - \delta(t_{\mathrm{c}})\sin\delta(t_{\mathrm{c}})) \\ - \eta_6(\delta(t_{\mathrm{u}})\cos\delta(t_{\mathrm{u}}) - \delta(t_{\mathrm{c}})\cos\delta(t_{\mathrm{c}})) \end{aligned} \tag{35}$$

where the subscripts D and P are defined in Section II; ξ_1—ξ_3 and η_1—η_6 in (33) and (35) are constants, with detailed equations given in the Appendix. The *SI*, which considers the dynamics of WPPs on the rotor angle stability, is then given as:

$$SI = \frac{A_{dec} - A_{acc}}{A_{acc}} \tag{36}$$

The following data are required to evaluate the expressions in (32)-(36): (a) system admittance matrix at $t_{\mathrm{f+}}$ and $t_{\mathrm{c+}}$, (b) rotor angles of each SG at t_{f} and t_{c}, (c) pre-fault internal voltage magnitudes of each SG, and (d) voltages of each POI at $t_{\mathrm{f+}}$ and $t_{\mathrm{c+}}$.

PMU-based fault location detection is introduced in [22], and online event and fault type detection are reported in [23]. These methods are determining factors to obtain values of (a). On the other hand, the pre-fault internal voltage of the SGs, the voltages of the POIs, and the rotor angles during and after the clearance of faults can be estimated from PMU measurements [24], [25]. Therefore, the *SI* can be calculated immediately after $t_{\mathrm{c+}}$. Based on (36), the value of the *SI* correlates with the stability margin of the post-fault network.

IV. The Proposed Solution Framework

Given the *SI* developed in Section III.C, a column vector $\boldsymbol{SI}$ is proposed and used as a feature for an ML technique to train an optimal stability prediction model. The $\boldsymbol{SI}$, shown in (37), consists of the *SI* values of all finite sets of feasible IMs of a certain system:

$$\boldsymbol{SI} = \left[SI^1 \;\; SI^2 \;\; \ldots \;\; SI^{|\Omega^{\mathrm{IM}}|}\right]^{\mathrm{T}} \tag{37}$$

where the Ω^{IM} represents the set of all feasible IMs of a certain system, i.e., each element in Ω^{IM} is a certain clustering pattern representing both the critical and remaining SGs.

Hence, with a pre-identified Ω^{IM}, an $\boldsymbol{SI}$ vector is calculated at $t_{\mathrm{c+}}$ in case of a contingency. Taking advantage of a set of $\boldsymbol{SI}$ vectors, an ML classifier algorithm is then applied for the training of a rotor angle stability prediction model.

The advantages of using the $\boldsymbol{SI}$ vectors as features include the following:

(1) *Features are more informative and discriminative*. Each element in the column vector correlates with the stability margin of each IM. Therefore, the proposed method has sufficient potential to outperform the existing ML-based stability prediction methods [3], [10]–[12], in which the features are the unprocessed data directly obtained from PMUs.

(2) *No online IM identification procedure is needed.* The IM identification, known as clustering of the critical and remaining SGs, provides the "reference coordinate" for calculations of *SIs* [8], [16], and an inaccurate online IM identification may lead to erroneous prediction results. However, existing online IM identification methods require long post-fault observation windows [26], [27], which may be impractical for real-life power systems that demand an extremely short time to trigger the emergency control action. Despite this, the Ω^{IM} of a real-life system can be pre-identified by analyzing offline simulations of various disturbances [9], during which each WPP can also be clustered into an associated SG coherent group as mentioned in Section III.A. Having Ω^{IM} for a specific system, in case of a contingency, the developed algorithm is employed in parallel to find *SI*s for all possible IMs to form an $\boldsymbol{SI}$ vector, and thus no online IM identification is needed.

(3) *More reliable prediction results are achieved.* In the proposed approach, each element in the $\boldsymbol{SI}$ vector is projected into a high dimensional space to search a hypersurface that separates the stable and unstable cases via an ML technique. Therefore, compared with identifying the instability either from a conservative or optimistic *SI* threshold value [8], [16], [28], the classifier hypersurface trained from the $\boldsymbol{SI}$ vector provides a more reliable prediction.

The process of the proposed framework consists of pre-identifying all possible IMs as the initial stage, followed by the formation of an $\boldsymbol{SI}$ vector and a model training process as the next stages.

To train the classifier, the rotor angle stability status of the offline simulations should be calculated and used as target labels. In this study, stability status is calculated at the end of each simulation as follows [12]:

$$\lambda_k = \frac{2\pi - \Delta\delta}{2\pi + \Delta\delta}, \qquad \forall\, k \in \Omega^{\mathrm{f}} \tag{38}$$

where $\Delta\delta$ is the maximum rotor angle deviation between any pair of SGs at the end of the simulation. Ω^{f} shows sets of all fault scenarios considered during the generation of training data, and λ_k indicates the final stability status of the fault scenario k, in which positive values indicate a stable network and negative otherwise.

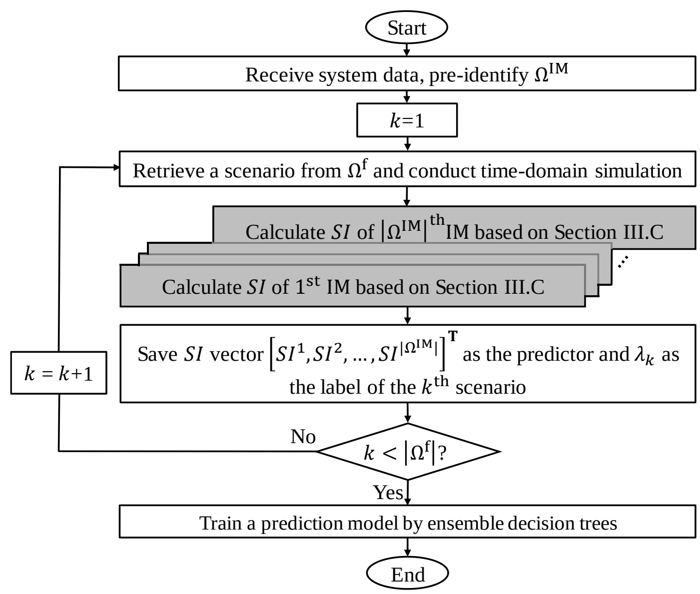

Fig. 4. The proposed framework.

In this study, ensemble decision tree (DT) is employed to process the *SI* vectors and find the optimal classifiers. DT is amongst the most prevalent non-parametric supervised classification techniques [29]. For ensemble DT, ensemble techniques are engaged to create a collection of features as multiple weighted DTs. It involves incrementally building an ensemble by training each new method instance to emphasize the training instances that previous methods misclassified. In this work, the DTs are built with the standard classification, and the ensembles are created based on the boosting technique [30]. Other classification techniques such as deep learning can also be applied without loss of generality.

The overall process of the proposed framework is shown in Fig.

4. As the grey area in this flowchart highlights, a major portion of the process can be solved in parallel, which substantially reduces the computational complexity.

V. Test and Results

To solve the stability prediction problem by the proposed method, the described framework is realized by a Python-based interface that calls PSS/E software [19] to carry out simulations, saves the database generated, and creates the prediction model.

IEEE 68-bus, 16-machine and 300-bus, 69-machine networks are employed and modified to perform the simulations. The configurations of the two networks are omitted and can be found in [31] and [32], respectively. Nine WPPs are installed at bus-18, -22, -25, -29, -31, -32, -36, -41, and -42 in the modified 68-bus network and 15 WPPs are installed at bus-84, -143, -190, -236, -241, -7002, -7003, -7012, -7017, -7024, -7039, -7061, -7130, -7139, and -7166 in the modified 300-bus network. All SGs in the networks are detailed 6th-order models and equipped with DC4B excitation systems. IEEEST stabilizers and IEESGO governors are installed for each SG. Therefore, the internal voltage magnitude and mechanical power of SGs vary during the transient simulations. It might be helpful to mention that these values are assumed to remain constant for simplicity in Sections II and III. Such a simplification is considered inside the developed method, but not the stability simulations. In addition, each WPP is modeled by an aggregated 1.5 MW DFIG model. All of these dynamic models are available in [19] and their parameters are noted in [19], [31], and [32]. The computer used in simulations featured an Intel 3.4-GHz CPU with 16 GB of RAM.

A. Database Generation

Database generation is required to validate the proposed framework. The training database is obtained from Monte Carlo time-domain simulations. To this end, reasonable uncertainty models, including outputs of WPPs, load levels, and fault locations and durations, are essential.

In practice, these uncertainty models can be statistically estimated from the corresponding historical observations. In this paper, the generation of each WPP, represented by 24 probability density functions (PDFs) that correspond to 24 hours of a day, are estimated using Gaussian kernels in a non-parametric way using hourly historical data from [33]. The same method is applied to each load where the historical data are retrieved from [34]. Thus, before running a dynamic simulation for a specific scenario, the hour of the day is sampled randomly and then each load and WPP outputs are sampled from its PDF of the sampled hour, and optimal power flow is then solved to balance the load and determine the output of each SG. Further, because SGs in the test networks are considered to be conventional power plants with aggregated units, the parameters of each SG are then adjusted based on their updated output. In brief, by increasing wind power penetration, some units in each conventional power plant are turned off, so the electrical parameters of each SG are adjusted accordingly, as discussed in [9]. Fault duration is randomly selected to be between 6 and 15 cycles [12]. The faults are assumed to be permanent and are cleared by switching out the faulted line. Moreover, faults are randomly applied to transmission lines for each simulation. Only three-phase faults are considered in this paper, though the proposed method is capable of handling other fault types as well. The above procedures are realized by a Python-based interface and the Monte Carlo simulations are carried out in PSS/E software, which provides the Python application programming interface (API).

Different wind power penetrations are also set for the two networks for testing. Wind power installed capacity ratio (WIC) in both test networks is increased from 0 to 50% of the total available capacity of SGs in increments of 10%; these scenarios are denoted as WIC0 to WIC50%, respectively. Finally, for each WIC scenario, 7000 and 35000 simulations are carried out in the two modified IEEE 68- and 300-bus networks, respectively.

The data simulated for offline analysis are shown in Table I, where the average pre-fault instantaneous wind power penetrations (AVG-IWP) of each WIC scenario are also given. The database is employed to perform the analyses in Sections V.B–V.D for different validation purposes.

Table I
Simulation Data of the Two Networks for Different Scenarios

WIC	Modified 68-bus network		Modified 300-bus network	
	Instability ratio	AVG-IWP	Instability ratio	AVG-IWP
0%	16.53%	-	12.91%	-
10%	11.84%	4.53%	12.13%	4.95%
20%	11.71%	9.17%	10.69%	9.77%
30%	12.80%	14.22%	11.51%	14.78%
40%	14.16%	18.37%	12.54%	19.40%
50%	14.81%	23.84%	14.27%	24.30%

B. Assessment of the Proposed SI

This subsection aims to assess (i) the validity of the virtual dynamic admittances developed in Section III and (ii) the effect of online misidentification of the IM on the accuracy of the *SI*.

For (i), the accuracy of the *SI* calculated with the dynamic admittances is compared with the accuracy calculated with static pre-fault WPP-equivalent admittances. It is worth noting that, in the static admittance scenario, the WPPs are equivalent to static admittances whose values are calculated by (17) using the pre-fault conditions. During transients, the dynamics of the WPPs are ignored, i.e., the values of the WPP-equivalent admittances remain unchanged. Thus, in case of a contingency, the EEAC as listed in (1)–(11) and (36) can be directly applied to calculate the *SI*.

For (ii), two different IM online identification settings are made for the two tests in (i): the IM is either assumed correctly identified for each case, or randomly selected from a set of patterns that may appear due to the fault line.

Therefore, four settings are designed for the *SI* calculation, as listed in Table II. The accuracy of the *SI*s obtained under the four settings is then assessed and compared with respect to different threshold values and WICs. For this purpose, the cases simulated on the modified 68-bus network for WIC10, 30, and 50% are employed for the validation. For each WIC scenario, the *SI* value is calculated for the 7000 cases under the four different settings in Table II. For the sake of assessment, the threshold value for stability prediction is increased from -1 to 1 in increments of 0.1, and cases with an *SI* value smaller (larger) than the threshold value will be predicted as unstable (stable). The accuracy is the ratio of the number of correctly predicted cases to the total number of cases (7000). The results are presented in Fig. 5.

Table II
Different Settings for *SI* Calculation

Settings	Modeling of WPPs	IM identification
S1	Static admittances	Randomly selected
S2	Static admittances	Correctly identified
S3	Dynamic admittance	Randomly selected
S4	Dynamic admittance	Correctly identified

Fig. 5 shows that increasing the WIC results in a decrease in the overall prediction accuracy. With the proposed *SI*, the average stability prediction accuracy is 91.38% with WIC=50%, which is 2.81% lower than the case with WIC=10%. Even so, the prediction accuracy of the proposed *SI* is markedly better than those in which the dynamic admittances are replaced by static ones in the *SI* calculation process; the average accuracy improvement for WIC10, 30, and 50% is 2.18, 5.17, and 8.71%, respectively. Such outcomes demonstrate the efficacy of the dynamic admittances on modeling the dynamics of WPPs, and validate the effectiveness of the proposed *SI* for cases with high penetration of wind power. Moreover, this figure shows that the accuracy is susceptible to the settings of the threshold value and, last but not least, that the misidentification of IM can degrade the overall accuracy. Hence, to further improve the accuracy, the proposed framework is applied, and its performance is illustrated in the following subsection.

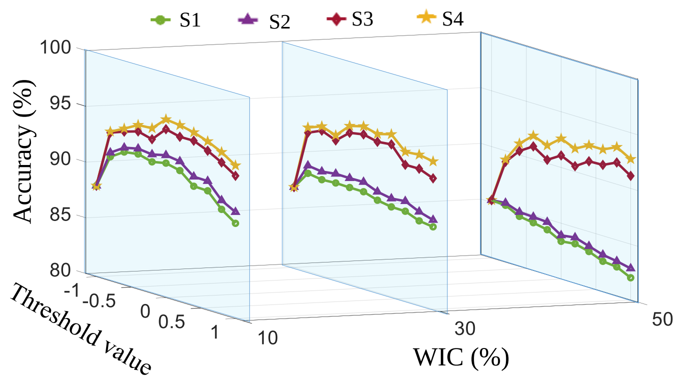

Fig. 5 The stability prediction accuracy of different techniques with respect to WICs for different threshold values.

C. Performance of the Proposed Stability Prediction Framework

To investigate the performance of the proposed framework with respect to different levels of wind power penetration and related uncertainties, the database shown in Table I is employed for testing. In each WIC scenario, 70% of the simulation cases are randomly chosen for training while the remainder are used in testing, this process is repeated 10 times and the average prediction accuracy is recorded. The training process explained in Section IV is conducted, and the results obtained are reported in Table III.

The performance of the proposed framework is also compared with state-of-the-art techniques in Table III. The most prevalent features, e.g., rotor angles δ [9], [10], [11], speeds ω [11], and terminal voltages of each SG, V_{SG} [3], [11] for before-, during-, and post-fault (at t_{f-}, t_{f+}, t_{c-} and continuous sampling for five cycles after t_c), are respectively employed to train the models for comparison purposes. For the sake of better comparison, all of the features are solved with an ensemble DT trained by the boosting technique.

Comparing the results obtained from the proposed framework with those using δ , ω, or V_{SG} clearly reveals the superiority of the *SI* vector for stability prediction; for the two test networks, the prediction accuracies of the proposed method averaged across the six WICs are 98.53 and 97.30%, which are better than those of using δ, ω, or V_{SG}. With increasing wind power penetration, the proposed method has a distinct advantage in terms of accuracy. This is because, compared to other features, each *SI* vector correlates with a set of stability margin indices considering the influences of WPPs on system dynamics. Notably, δ, ω, and V_{SG} require five cycles of post-fault data, which means they respond 83.3 ms later than the proposed method.

TABLE III
COMPARISON OF THE PREDICTION ACCURACY FOR DIFFERENT FEATURES USING AN ENSEMBLE DT

WIC	Modified 68-bus network				Modified 300-bus network			
	δ	ω	V_{SG}	**Proposed**	δ	ω	V_{SG}	**Proposed**
0%	95.74%	97.96%	98.09%	**99.03%**	89.86%	93.27%	95.08%	**98.04%**
10%	93.61%	97.05%	96.88%	**98.98%**	88.24%	92.24%	93.84%	**97.87%**
20%	92.59%	95.38%	95.79%	**98.59%**	84.97%	89.52%	90.81%	**97.61%**
30%	92.18%	94.82%	94.42%	**98.46%**	83.49%	86.84%	89.26%	**97.26%**
40%	91.14%	92.06%	92.29%	**98.17%**	81.29%	84.19%	87.79%	**96.83%**
50%	89.56%	91.24%	91.35%	**97.96%**	78.34%	83.14%	85.35%	**96.17%**

In addition, the prediction accuracy is evaluated for different combinations of the existing features and the results obtained are reported in Table IV. Comparing Table IV and Table III shows that combining the features generally improves the prediction accuracy, while a noticeable gap still exists compared to utilizing the *SI* vector, especially in high wind power-integrated scenarios. The results show that interpreting these raw data into derived features effectively improves the accuracy of the ML-based prediction model. It should be noted that an increase in the number of features could lead to an overfitting issue, which may subsequently lead to a degradation in overall performance [12], [14], i.e., Table IV shows the accuracy may worsen when using all three features compared to only using ω and V_{SG}. Considering the number of features can be relatively high for large-scale networks by simply combining all available features, it is vital to reduce the dimensionality of the input space and consequently improve the generalization performance of the classifier [12].

TABLE IV
COMPARISON OF THE PREDICTION ACCURACY FOR DIFFERENT SETS OF INPUT FEATURES USING AN ENSEMBLE DT

WIC	Modified 68-bus network				Modified 300-bus network			
	δ+ω	δ+V_{SG}	ω+V_{SG}	δ+ω+V_{SG}	δ+ω	δ+V_{SG}	ω+V_{SG}	δ+ω+V_{SG}
0%	98.02%	98.10%	99.11%	99.10%	93.21%	95.01%	97.06%	96.99%
10%	96.69%	96.51%	97.36%	97.11%	92.27%	93.57%	94.02%	94.22%
20%	94.96%	95.98%	96.03%	96.01%	89.42%	89.54%	91.45%	91.39%
30%	94.65%	95.00%	95.13%	95.25%	86.52%	88.33%	90.63%	90.71%
40%	92.32%	92.25%	93.51%	93.26%	85.85%	87.50%	89.54%	89.30%
50%	91.15%	91.03%	92.34%	92.36%	85.11%	87.02%	88.99%	88.86%

Besides the boosting technique-trained ensemble DT, different prediction engines, including neural network (NN), support vector machine (SVM), and random forest (RF) are also applied to test the performance of each feature. In this comparison, the two networks for WIC50% are employed and all prediction engines are trained using the *scikit-learn* 0.20.4 package [35] in Python. The results noted in Table V show the *SI* vector still outperforms the others while the accuracies of each features vary somewhat compared to corresponding results in Table III. Specifically, the tree-based algorithms (boosting technique-trained ensemble DT, RF) show advantages in rotor angle stability prediction, which corroborates the simulation results in [10].

TABLE V
COMPARISON OF THE PREDICTION ACCURACY FOR DIFFERENT SETS OF INPUT FEATURES USING DIFFERENT ML TECHNIQUES

Algorithm	Modified 68-bus network (WIC50%)				Modified 300-bus network (WIC50%)			
	δ	ω	V_{SG}	***SI* vector**	δ	ω	V_{SG}	***SI* vector**
NN	91.03%	91.60%	91.02%	**96.13%**	77.30%	84.36%	85.66%	**95.56%**
SVM	90.04%	91.36%	91.12%	**95.93%**	78.34%	82.81%	84.05%	**94.75%**
RF	90.46%	92.30%	91.33%	**97.52%**	79.51%	85.15%	87.63%	**96.68%**

Furthermore, to better illustrate the advantages of using *SI* vectors as features, the distribution of simulation samples in SI space and the performance of the proposed method with respect to dimensions of each SI vector are shown in Fig. 6 and Fig. 7, respectively. The samples are simulated from the aforesaid IEEE 68-machine network for WIC50%, during which 18 IMs are identified, as listed in Table VI in the order of the most to least prominent, based on the database. Similarly, the values in each SI vector are also sorted in the same order, and thus SI_1 ~ SI_3 is calculated based on the three most prominent IMs, respectively, in which the S/A cluster of SGs is No. 1 ~ 3 in Table VI, respectively. The two figures indicate that samples with lower SI values are more prone to instability, and the prediction accuracy improves by developing the dimension of the SI vector. Fig. 7 also shows that as the dimension of each SI vector develops to a certain level (e.g., 16), an increase in dimension of each SI vector does not significantly affect the prediction accuracy. This indicates that, in practice, the proposed method has enough potential to accurately predict stability status in cases where IMs rarely appear in the training phase.

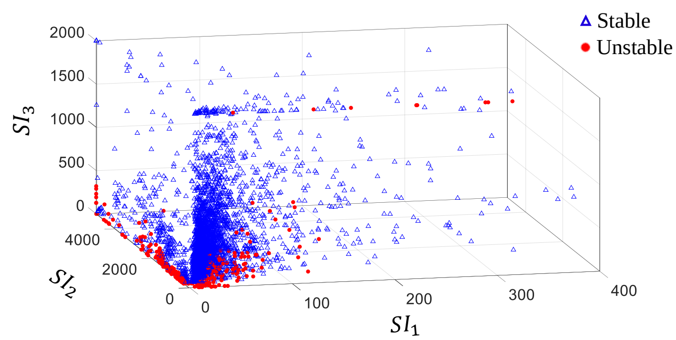

Fig. 6. Distribution of simulation samples in the SI_1, SI_2, and SI_3 planes.

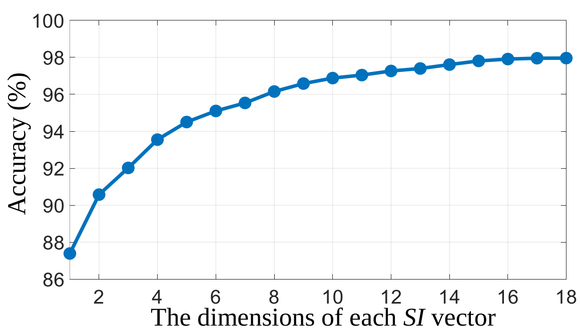

Fig. 7. Performance of the proposed method with respect to dimensions of each SI vector.

TABLE VI
IMS IDENTIFIED IN TRAINING DATABASE FOR THE IEEE 68-BUS TEST NETWORK FOR WIC50%

No.	Clustering of SGs (S/A)	No.	Clustering of SGs (S/A)
1	(G9)/(G1–G9, G10–G16)	10	(G1–G12)/(G13–G16)
2	(G14–16)/(G1–G13)	11	(G8)/(G1–G7, G9–G16)
3	(G1–G12, G14–G16)/(G13)	12	(G1–G9)/(G10–G16)
4	(G6–G7)/(G1–G5, G8–G16)	13	(G4–G7)/(G1–G3, G8–G16)
5	(G16)/(G1–G15)	14	(G1–G11)/(G12–G16)
6	(G11)/(G1-G10, G12–G16)	15	(G2–G7)/(G1, G8–G16)
7	(G8–G9)/(G1–G7, G10–G16)	16	(G3)/(G1–G2, G4–G16)
8	(G14)/(G1-G13, G15-G16)	17	(G2–G9)/(G1, G10–G16)
9	(G2–G3)/(G1, G4–G16)	18	(G1–10)/(G11–G16)

D. *Sensitivity Analysis with Respect to Practical Issues*

The robustness of an algorithm should be assessed by its sensitivity to discrepancies among the assumed scenarios and reality. In practice, the behavior of some uncertainties may differ from those considered in the training process, e.g., when WPPs are exposed to abnormal weather. In addition, the topology of the networks may vary in real scenarios for different operations. These uncontrollable factors may interfere with the prediction results from a trained model. For this reason, two prediction models that are already trained by ensemble DT from the aforesaid two networks for WIC50% are employed for the robustness test.

In the first robustness test (RT-I), the two trained models are tested using data simulated from the corresponding network while the PDFs for each WPP are trained from another data source from [36]. In this paper, the Wasserstein Distance (WD) is used to measure the difference between the original and modified PDFs of each WPP. This distance function can be defined between probability distributions μ and υ, as follows [37]:

$$W(\mu,\upsilon) = \inf_{\pi\in\Phi(\mu,\upsilon)} \int_{\mathbb{R}\times\mathbb{R}} |x-y| d\pi(x,y) \tag{39}$$

where $\Phi(\mu,\upsilon)$ is the set of probability distributions on $\mathbb{R}\times\mathbb{R}$ whose marginals are μ and υ on the first and second factors, respectively. The WDs between new PDFs of each WPP and corresponding originals of the modified 68-bus network are listed in Table VII. The WDs of the 300-bus network are omitted due to space limitations; all values are between 0.1 and 0.4.

TABLE VII
WD BETWEEN NEW PDFS OF EACH WPP AND CORRESPONDING ORIGINALS

WPP Connected Bus	18	22	25	29	31	32	36	41	42
WD	0.32	0.33	0.31	0.09	0.33	0.40	0.29	0.25	0.39

In the second robustness test (RT-II), the two trained models are tested using data simulated from the corresponding network under randomly $N-1$ conditions, i.e., one of the elements of the network is randomly switched out before each dynamic simulation.

7000 and 35000 cases are respectively simulated from the two networks based on the database generation method introduced in Section V.A for both RT-I and RT-II. The two trained models applied to test these data and their performance is compared with accuracies predicted by V_{SG}, which performs relatively better than δ or ω with respect to prediction accuracy according to Table III. The results are illustrated in Fig. 8.

Fig. 8 shows that the prediction accuracies based on V_{SG} are vulnerable to the profile of probability distributions used to represent the system uncertainties and susceptible to changes in the system typology, while the proposed method demonstrates better robustness. This is because the calculation of SI vectors takes system operating points such as real-time topology and wind power penetration into consideration. This validates the robustness of the proposed method with respect to abnormal weather and variations in network typology.

The performance of the proposed method is also assessed in the presence of PMU measurement errors. According to the IEEE C37.118 standard [38], the PMU measurements should have a total vector error of less than 1%. To this end, following the approach in [3], white noise is generated and imposed on all post-fault offline data listed in Table I, and the training and testing process is repeated. The results are reported in Table VIII. Compared to the results when PMU measurement errors are ignored, the average accuracies of the two networks in all WICs decrease by 0.74 and 0.98%, respectively. To conclude, the proposed method can make high quality predictions considering noisy PMU measurements.

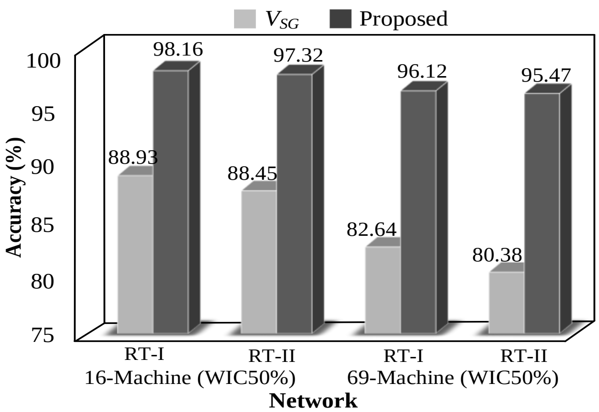

Fig. 8. Performance of the proposed framework in robustness tests.

TABLE VIII
PREDICTION ACCURACY OF THE PROPOSED METHOD CONSIDERING PMU MEASUREMENT ERRORS

WIC	0%	10%	20%	30%	40%	50%
Modified 68-bus network	98.21%	97.86%	97.73%	97.62%	97.32%	97.13%
Modified 300-bus network	97.16%	96.91%	96.48%	96.23%	95.86%	95.24%

The performance of the proposed method is also investigated with respect to the size of the training database. To do so, a set of offline scenarios is randomly selected and an ensemble DT is employed to train the prediction model. For each specific size of training database, this process is repeated 10 times and the average prediction accuracies are illustrated in Fig. 9. This figure shows an adequate database is essential to train an accurate prediction model, and the performance changes slightly when the database reaches a certain level. Based on Fig. 9, the size of the databases used for the two networks (7000 and 35000, respectively) in this paper seems adequate.

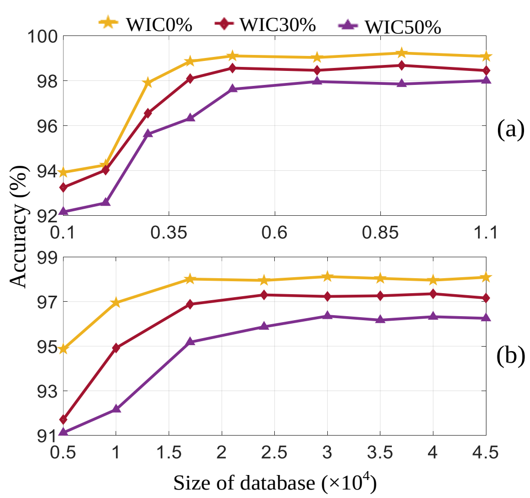

Fig. 9. Performance of the proposed framework with respect to the size of the training database. Tests are conducted on the (a) modified 68- and (b) 300-bus networks.

VI. CONCLUSION

This paper proposes a novel approach for rotor angle stability prediction of power systems in the presence of high penetration of wind power. The framework first develops a new stability index, in which the dynamic behavior of WPPs is taken into account. Inspired by EEAC- and PMU-related studies, an approach is then put forward in which the developed algorithm is employed in parallel to find *SI*s for all possible IMs layouts; *SI* vectors are then constructed and selected as features for rotor angle stability prediction. The effectiveness of the proposed approach is validated by ensemble decision trees on two IEEE test systems at different wind power penetration levels. The results obtained and comparisons reported reveal the superiority of the proposed approach in terms of accuracy, speed, and robustness.

REFERENCES

[1] P. Kundur *et al.*, “Definition and classification of power system stability,” *IEEE Trans. Power Syst.*, vol. 19, pp. 1387–1401, May. 2004.

[2] P. M. Anderson and A. A. Fouad, *Power System Control and Stability*, New York, NY, USA: IEEE Press, 2003.

[3] J. J. Q. Yu, D. J. Hill, A. Y. S. Lam, J. Gu, and V. O. K. Li, “Intelligent time-adaptive transient stability assessment system,” *IEEE Trans. Power Syst.*, vol. 33, no. 1, pp. 1049–1058, Jan. 2018.

[4] M. A. Pai, K. R. Padiyar, and C. RadhaKrishna, “Transient stability analysis of multi-machine AC/DC power systems via energy-function method,” *IEEE Trans. Power App. Syst.*, vol. PAS-100, no. 12, pp. 5027–5035, Dec. 1981

[5] A. N. Michel, A. A. Fouad and V. Vittal, “Power system transient stability using individual machine energy functions”, *IEEE Trans. Circuits Syst.*, Vol. CAS-30, no. 5, pp. 266–276, May. 1983.

[6] N. A. Tsolas, A. Arapostathis, and P.P.Varaiya, “A structure preserving energy function for power system transient stability analysis,” *IEEE Trans. Circuits Syst.*, vol. CAS-32, no. 10, pp. 1041–1049, Oct. 1985.

[7] H.D.Chiang, F.F. Wu, and P.P. Varaiya. “Foundations of direct methods for power system transient stability analysis,” *IEEE Trans. Circuits Syst.*, vol. 34, no. 2, pp. 160–173, Feb. 1987.

[8] Y. Xue, T. Van Cutsem, and M. Ribbens-Pavella, “A simple direct method for fast transient stability assessment of large power systems,” *IEEE Trans. Power Syst.*, vol. 3, no. 2, pp. 400–412, 1988.

[9] P. N. Papadopoulos, T. Guo, and J. V. Milanovic, “Probabilistic framework for online identification of dynamic behavior of power systems with renewable generation,” *IEEE Trans. Power Syst.*, vol. 33, no. 1, pp. 45-54, Jan. 2018.

[10] T. Guo, S. Member, and J. V Milanović, “Online identification of power system dynamic signature using PMU measurements and data mining,” *IEEE Trans. Power Syst.*, vol. 31, no. 3, pp. 1760–1768, May. 2016.

[11] Y. Tang, F. Li, Q. Wang, and Y. Xu, “Hybrid method for power system transient stability prediction based on two-stage computing resources,” *IET Gener. Transm. Dis.*, vol. 12, no. 8, pp. 1697–1703, Apr. 2018.

[12] S. M. Mazhari, N. Safari, C. Y. Chung, and I. Kamwa, “A hybrid fault cluster and thevenin equivalent based framework for rotor angle stability prediction,” *IEEE Trans. Power Syst.*, vol. 33, no. 5, pp. 5594–5603, Jul. 2018.

[13] J. Bosch, I. Staffell, and A. D. Hawkes, “Temporally-explicit and spatially-resolved global onshore wind energy potentials,” *Energy.*, vol. 131, pp. 207–217, Jul. 2017.

[14] J. P. Barddal, H. M. Gomes, and F. Enembreck, “Analyzing the Impact of Feature Drifts in Streaming Learning,” in *Proc. ICONIP*, Istanbul, Turkey, 2015, pp. 21–28.

[15] R. Ghiga, K. Martin, Q. Wu, and A. H. Nielsen, “Phasor Measurement Unit Test under Interference Conditions,” *IEEE Trans. Power Deliv.*, vol. 33, no. 2, pp. 630–639, Apr. 2018.

[16] Y. Xue, T. Van Cutsem, and M. Ribbens-Pavella, “Extended equal area criterion justifications, generalizations, applications,” *IEEE Trans. Power Syst.*, vol. 4, no. 1, pp. 44–52, Feb. 1989.

[17] A. M. Khalil and R. Iravani, “Power system coherency identification under high depth of penetration of wind power,” *IEEE Trans. Power Syst.*, vol. 33, no. 5, pp. 5401–5409, Sep. 2018.

[18] *WECC Wind Plant Dynamic Modeling Guidelines*, May 2014, [online] Available: https://www.wecc.org/reliability/wecc%20wind%20plant%20dynamic%20modeling%20guidelines.pdf

[19] Siemens Power Technologies International, PSS®E 34.2 Program Application Guide: Volume 2, Apr 2017.

[20] D. Wang, H. Wang, J. Jia, and Y. Zhang, “Reactive power control of doubly fed induction generator in wind farm under low grid voltage,” in *Proc., CRIS 2010*, Beijing, China, 2010, pp. 1–6.

[21] Y. Lei, A. Mullane, G. Lightbody, and R. Yacamini, “Modeling of the wind turbine with a doubly fed induction generator for grid integration studies,” *IEEE Trans. Energy Convers.*, vol. 21, no. 1, pp. 257–264, Mar. 2006.

[22] J.W. Lee, W.K Kim, J. Han, and W.H. Jang, C.H Kim, “Fault area estimation using traveling wave for wide area protection,” *J. Mod. Power Syst. Clean Energy*, vol. 4, no. 3, pp. 478–486, Jul. 2016.

[23] P. Bhui and N. Senroy, "Online identification of tripped line for transient stability assessment," *IEEE Trans. Power Syst.*, vol. 31, no. 3, pp. 2214–2224, May. 2016.

[24] S. Wei, M. Yang, J. Qi, J. Wang, S. Ma, and X. Han, "Model-free MLE estimation for online rotor angle stability assessment with PMU data," *IEEE Trans. Power Syst.*, vol. 33, no. 3, pp. 2463–2476, May. 2018.

[25] A. G. Phadke and B. Kasztenny, "Synchronized phasor and frequency measurement under transient conditions," *IEEE Trans. Power Deliv.*, vol. 24, no. 1, pp. 89–95, Jan. 2009.

[26] Z. Lin, F. Wen, Y. Ding, and Y. Xue, "Data-driven coherency identification for generators based on spectral clustering," *IEEE Trans. Ind. Informatics*, vol. 14, no. 3, pp. 1275–1285, Mar. 2018.

[27] J. Wei, D. Kundur, and K. L. Butler-Purry, "A novel bio-inspired technique for rapid real-time generator coherency identification," *IEEE Trans. Power Syst.*, vol. 6, no. 1, pp. 178–188, Jan. 2015.

[28] D. Rimorov, X. Wang, I. Kamwa, and G. Joos, "An approach to constructing analytical energy function for synchronous generator models with subtransient dynamics," *IEEE Trans. Power Syst.*, vol. 33, no. 6, pp. 5958–5967, Nov. 2018.

[29] L. Breiman, J. H. Friedman, R. A. Olshen, and C. J. Stone, "Classification and regression trees," *Wadsworth & Brooks Monterey*, CA, 1984.

[30] Y. Freund and R. E. Schapire, "A decision-theoretic generalization of on-line learning and an application to boosting," *J. Comput. Syst. Sci.*, vol. 55, no. 1, pp. 119–139, 1997.

[31] A. K. Singh and B. C. Pal, "Report on the 68-bus, 16-machine, 5-area system," *IEEE PES Task Force on Benchmark Systems for Stability Controls,* Ver. 3.3, 2013.

[32] R. Zimmerman C. E. Murillo-Sánchez, and R. J. Thomas, "MATPOWER steady-state operations, planning and analysis tools for power systems research and education," *IEEE Trans. Power Syst.*, vol. 26, no. 1, pp. 12–19, Feb. 2011.

[33] T. Hong, P. Pinson, S. Fan, H. Zareipour, A. Troccoli, and R. J. Hyndman, "Probabilistic energy forecasting: Global Energy Forecasting Competition 2014 and beyond," *Int. J. Forecast.*, vol. 32, no. 3, pp. 896–913, Jul. 2016.

[34] Data download from the website: http://www.pjm.com/markets-and-operations/ops-analysis/historical-load-data.aspx.

[35] F. Pedregosa *et al.*, "Scikit-learn: Machine learning in python," *J. Mach. Learn. Res.*, vol. 12, no. Oct, pp. 2825–2830, 2011.

[36] Data download from the website: https://setis.ec.europa.eu/EMHIRES-datasets.

[37] C. Wang, R. Gao, F. Qiu, J. Wang, and L. Xin, "Risk-based distributionally robust optimal power flow with dynamic line rating," *IEEE Trans. Power Syst.*, vol. 33, no. 6, pp. 6074–6086, Jun. 2018.

[38] *IEEE Standard for Synchrophasor Data Transfer for Power Systems*, IEEE Std. C37.118.2-2011, Dec. 2011

APPENDIX

For simplicity, assume that during fault period the value of $\boldsymbol{V}$ can be considered as $\boldsymbol{V}(t_{\mathrm{f+}})$; thus given (8)–(9), (15)–(18), (28), and (32)–(35), ξ_1– ξ_3 can be derived as (40)–(42). During the fault period, the real-time value of $\boldsymbol{V}$, which is obtainable from PMUs, can also be used for calculating (10) without loss of generality. η_1– η_6 are derived as (43)-(48).

$$\xi_1 = \frac{M_A}{M_T}\boldsymbol{E_S}^{\mathrm{T}}\mathrm{Re}(\boldsymbol{Y}_{SG}(t_{\mathrm{f+}}))\boldsymbol{V}_G(t_{\mathrm{f+}}) - \frac{M_S}{M_T}\boldsymbol{E}_A{}^{\mathrm{T}}\mathrm{Re}(\boldsymbol{Y}_{AH}(t_{\mathrm{f+}}))\boldsymbol{V}_H(t_{\mathrm{f+}}) \tag{40}$$

$$\xi_2 = \frac{M_A}{M_T}\boldsymbol{E}_S{}^{\mathrm{T}}\mathrm{Re}(\boldsymbol{Y}_{SH}(t_{\mathrm{f+}}))\boldsymbol{V}_H(t_{\mathrm{f+}}) - \frac{M_S}{M_T}\mathbf{E}_A{}^{\mathrm{T}}\mathrm{Re}(\boldsymbol{Y}_{AG}(t_{\mathrm{f+}}))\boldsymbol{V}_G(t_{\mathrm{f+}}) \tag{41}$$

$$\xi_3 = \frac{M_A}{M_T}\boldsymbol{E}_S{}^{\mathrm{T}}\mathrm{Im}(\boldsymbol{Y}_{SH}(t_{\mathrm{f+}}))\boldsymbol{V}_H(t_{\mathrm{f+}}) - \frac{M_S}{M_T}\mathbf{E}_A{}^{\mathrm{T}}\mathrm{Im}(\boldsymbol{Y}_{AG}(t_{\mathrm{f+}}))\boldsymbol{V}_G(t_{\mathrm{f+}}) \tag{42}$$

$$\eta_1 = \frac{M_S}{M_T}\boldsymbol{E}_A{}^{\mathrm{T}}\mathrm{Re}(\boldsymbol{Y}_{AH}(t_{\mathrm{c+}}))\big(\boldsymbol{V}_H(t_{\mathrm{c+}}) - \boldsymbol{K}_H\delta(t_{\mathrm{c}})\big) - \frac{M_A}{M_T}\boldsymbol{E}_S{}^{\mathrm{T}}\mathrm{Re}(\boldsymbol{Y}_{SG}(t_{\mathrm{c+}}))\big(\boldsymbol{V}_G(t_{\mathrm{c+}}) - \boldsymbol{K}_G\delta(t_{\mathrm{c}})\big) \tag{43}$$

$$\eta_2 = \frac{M_S}{2M_T}\boldsymbol{E}_A{}^{\mathrm{T}}\mathrm{Re}(\boldsymbol{Y}_{AH}(t_{\mathrm{c+}}))\boldsymbol{K}_H - \frac{M_A}{2M_T}\boldsymbol{E}_S{}^{\mathrm{T}}\mathrm{Re}(\mathbf{Y}_{SH}(t_{\mathrm{c+}}))\boldsymbol{K}_H \tag{44}$$

$$\eta_3 = \frac{M_S}{M_T}\boldsymbol{E}_A{}^{\mathrm{T}}\mathrm{Re}\big(\boldsymbol{Y}_{AG}(t_{\mathrm{c+}})\big)\big(\boldsymbol{V}_G(t_{\mathrm{c+}}) - \boldsymbol{K}_G\delta(t_{\mathrm{c}})\big) + \frac{M_A}{M_T}\boldsymbol{E}_S{}^{\mathrm{T}}\mathrm{Re}\big(\boldsymbol{Y}_{SH}(t_{\mathrm{c+}})\big)\big(\boldsymbol{K}_H\delta(t_{\mathrm{c}}) - \boldsymbol{V}_H(t_{\mathrm{c+}})\big) \tag{45}$$

$$\eta_4 = \frac{M_S}{M_T}\boldsymbol{E}_A{}^{\mathrm{T}}\mathrm{Im}\big(\boldsymbol{Y}_{AG}(t_{\mathrm{c+}})\big)\big(\boldsymbol{V}_G(t_{\mathrm{c+}}) - \boldsymbol{K}_G\delta(t_{\mathrm{c}})\big) + \frac{M_A}{M_T}\boldsymbol{E}_S{}^{\mathrm{T}}\mathrm{Im}\big(\boldsymbol{Y}_{SH}(t_{\mathrm{c+}})\big)\big(\boldsymbol{V}_H(t_{\mathrm{c+}}) - \boldsymbol{K}_H\delta(t_{\mathrm{c}})\big) \tag{46}$$

$$\eta_5 = \frac{M_S}{M_T}\boldsymbol{E}_A{}^{\mathrm{T}}\mathrm{Re}(\boldsymbol{Y}_{AG}(t_{\mathrm{c+}}))\boldsymbol{K}_G - \frac{M_A}{M_T}\boldsymbol{E}_S{}^{\mathrm{T}}\mathrm{Re}(\boldsymbol{Y}_{SH}(t_{\mathrm{c+}}))\boldsymbol{K}_H \tag{47}$$

$$\eta_6 = -\frac{M_S}{M_T}\boldsymbol{E}_A{}^{\mathrm{T}}\mathrm{Im}\big(\boldsymbol{Y}_{AG}(t_{\mathrm{c+}})\big)\boldsymbol{K}_G - \frac{M_A}{M_T}\boldsymbol{E}_S{}^{\mathrm{T}}\mathrm{Im}\big(\boldsymbol{Y}_{SH}(t_{\mathrm{c+}})\big)\boldsymbol{K}_H \tag{48}$$

Y. Chen received the B.S. and M.S. degree from South China University of Technology, Guangzhou, China, in 2013 and 2016 respectively. Currently, he is pursuing the Ph.D. degree at the University of Saskatchewan, Saskatoon, SK, Canada. From January to May 2019, He was a visiting research student at Imperial College London, London, U.K. His research interests include applications machine learning algorithms in integration of renewable energy generation to power systems.

S.M. Mazhari (S'12-M'17) received his M.Sc. (Hon.) degree from the University of Tehran, Tehran, Iran, in 2012, and the Ph.D. (Hon.) degree from the Amirkabir University of Technology, Tehran, Iran, in 2016, all in electrical engineering. Currently, he is a postdoctoral research fellow at the University of Saskatchewan, Saskatoon, SK, Canada.

C.Y. Chung (M'01-SM'07-F'16) received the B.Eng. (with First Class Honors) and Ph.D. degrees in electrical engineering from The Hong Kong Polytechnic University, Hong Kong, China, in 1995 and 1999, respectively.

He is currently a Professor, the NSERC/SaskPower (Senior) Industrial Research Chair in Smart Grid Technologies, and the SaskPower Chair in Power Systems Engineering in the Department of Electrical and Computer Engineering at the University of Saskatchewan, Saskatoon, SK, Canada.

Dr. Chung is currently the Vice Editor-in-Chief of "Journal of Modern Power Systems and Clean Energy", Subject Editor of "IET Generation, Transmission & Distribution", Editor of "IEEE Transactions on Power Systems", "IEEE Transactions on Sustainable Energy", and "IEEE Power Engineering Letters", and Editorial Board Member of "CSEE Journal of Power and Energy Systems" and "Protection and Control of Modern Power Systems". He is also an IEEE PES Distinguished Lecturer and a member of IEEE PES Fellows Evaluation Committee.

Sherif O. Faried (S'88–M'88–SM'00) received the B.Sc. and M.Sc. degrees from Ain Shams University, Cairo, Egypt, in 1979 and 1984, respectively, and the M.Sc. and Ph.D. degrees from the University of Saskatchewan, Saskatoon, SK, Canada, in 1988 and 1993, respectively, all in electrical engineering.

From 1979 to 1984, he was a Teaching and Research Assistant with the Department of Electrical Power and Machines, Ain Shams University. He is currently a Professor of Electrical Engineering with the Department of Electrical and Computer Engineering, University of Saskatchewan. His current research interests include power system dynamics, control, reliability, protection, and power quality.

Prof. Faried is a Registered Professional Engineer in the Province of Saskatchewan, Canada.

Bikash C. Pal (M'00-SM'02-F'13) received B.E.E. (with honors) degree from Jadavpur University, Calcutta, India, M.E. degree from the Indian Institute of Science, Bangalore, India, and Ph.D. degree from Imperial College London, London, U.K., in 1990, 1992, and 1999, respectively, all in electrical engineering.

Currently, he is a Professor in the Department of Electrical and Electronic Engineering, Imperial College London. His current research interests include renewable energy modelling and control, state estimation, and power system dynamics.

He is Vice President Publications, IEEE Power & Energy Society. He was Editor-in-Chief of IEEE Transactions on Sustainable Energy (2012-2017) and Editor-in-Chief of IET Generation, Transmission and Distribution (2005- 2012) and is a Fellow of IEEE for his contribution to power system stability and control.